Journal of Inorganic and Organometallic Polymers and Materials (2018) 28:1276–1285
https://doi.org/10.1007/s10904-018-0828-5

Facile Solvothermal Synthesis of Novel $CuCo_2S_4$/g-C_3N_4 Nanocomposites for Visible-Light Photocatalytic Applications

S. Hariganesh[1] · S. Vadivel[1] · D. Maruthamani[1] · M. Kumaravel[1] · Aziz Habibi-Yangjeh[2]

Received: 18 November 2017 / Accepted: 14 March 2018 / Published online: 17 March 2018

Abstract
In this work, we synthesized a series of $CuCo_2S_4$/g-C_3N_4 (CSC) nanocomposites by a facile solvothermal approach using D-penicillamine as sulphur source. The phase structure, morphology, chemical composition, and optical properties were characterized by X-ray diffraction (XRD), scanning electron microscopy (SEM), high resolution transmission electron microscopy (HR-TEM), X-ray photoelectron spectroscopy (XPS), UV–vis diffuse reflectance spectroscopy (UV–vis DRS). The photocatalytic activities of the synthesized CSC nanocomposites were evaluated using degradation of methylene blue (MB) dye under visible-light irradiation. The light absorption capacity and photocatalytic activity of $CuCo_2S_4$ were enhanced by the successful incorporation with g-C_3N_4. The nanocomposite with 30% loading of g-C_3N_4 in $CuCo_2S_4$ exhibited maximum degradation efficiency compared to the pure $CuCo_2S_4$ towards the degradation of MB dye under the light irradiation. A possible mechanism for enhanced photocatalytic activity towards the pollutant degradation by the nanocomposites was proposed.

Keywords G-C_3N_4 · $CuCo_2S_4$ · D-penicillamine · Photocatalyst · Nanocomposite

1 Introduction

At present, the survival of the human society is threatened by various forms of organic pollutants and water scarcity. Water pollution due to rapid industrialization is one of the most severe problems associated with the depletion of fresh water resources. Improper discharges of dyes, pesticides, personal care products, pharmaceutical effluents, and etc. are the major sources of water pollutants [1–4]. Among the various wastewater treatment processes, advanced oxidation processes have been proven to be the efficient method for the degradation of pollutants in wastewater. In the past few decades, the semiconductors like TiO_2 [5] and ZnO [6] have been extensively applied in photocatalytic processes, due to their unique properties like non-toxicity and photostability. Nonetheless, these materials possess insufficient separation efficiency for the photoinduced electron–hole pairs and poor visible-light absorption ability and so they were excluded from the practical applications. In order to utilize more visible-light illumination, which constitutes large part of the solar spectrum, materials with narrow band gaps are preferred [7–9]. Nowadays, extensive researches have been carried out in this field to design more efficient photocatalysts with substantial activity under the solar illumination.

Recently, various metal sulphides such as $CuInS_2$ [10], Cu_2ZnSnS_4 [11], $SnCoS_4$ [12] and $CuSnS_3$ [13] have been extensively studied in the field of energy and environment. Among them, $CuCo_2S_4$, a binary metal sulphide photocatalyst has recently emerged in various energy storage applications, due to its unique electrical, magnetic, and catalytic properties [14]. To decrease high recombination rate of the photoexcited charge carriers in $CuCo_2S_4$, it should be combined with another appropriate semiconductors having matched band energies. Since 2009, it was found that graphitic carbon nitride (g-C_3N_4) is a metal-free semiconductor with high photocatalytic performance under visible light. Facile synthesis, good physicochemical stability, and narrow band gap of 2.7 eV are appealing properties of g-C_3N_4 to be a promising photocatalyst to address energy and environmental crises [15, 16]. Recently, many studies revealed that g-C_3N_4 incorporated semiconductors show good degradation efficiency than commercial ZnO and TiO_2 photocatalysts. In this light, many heterojunction photocatalysts

✉ S. Vadivel
vlvelu7@gmail.com

[1] Department of Chemistry, PSG College of Technology, Coimbatore, Tamilnadu 641004, India

[2] Department of Chemistry, Faculty of Science, University of Mohaghegh Ardabili, P.O. Box 179, Ardabil, Iran

such as $CaFe_2O_4$/g-C_3N_4 [17], $Co_{0.5}Cd_{0.5}S$/g-C_3N_4 [18], $CuCr_2O_4$/g-C_3N_4 [19], and Ag_2WO_4/g-C_3N_4 [20] have been successfully applied in the photocatalytic processes.

In this work, we have prepared $CuCo_2S_4$/g-C_3N_4 nanocomposites by a simple solvothermal method using D-penicillamine as sulphur source. The fabricated photocatalysts was applied for photocatalytic degradation of methylene blue (MB) under visible-light illumination and the improved activity was obtained for the nanocomposite relative to the pure $CuCo_2S_4$. To the best of our knowledge, there is not any report about photocatalytic activity of $CuCo_2S_4$/g-C_3N_4 nanocomposites under visible light.

2 Experimental

2.1 Synthesis of g-C_3N_4

Ten grams of melamine was placed in a semi closed silica crucible and heated at 550 °C in a muffle furnace in air atmosphere for 4 h to obtain a pale yellow powder and finally washed with dil. HNO_3 for further use [17].

2.2 Synthesis of $CuCo_2S_4$/g-C_3N_4 Nanocomposites (CSC)

The CSC nanocomposites were synthesized by simple solvothermal method. Stochiometric amount of synthesized g-C_3N_4 was dispersed in 40 ml of ethylene glycol through ultrasonication process for 30 min by a digital ultrasonic cleaner (bath type, India), with power of 150W and frequency of 40 kHz. Then 1 mmol of $Cu(NO_3)_2{\cdot}3H_2O$, 2 mmol of $Co(NO_3)_2{\cdot}6H_2O$ and 4 mmol of D-penicillamine were added into above suspension with continuous stirring for 30 min under room temperature. Finally the mixture was transferred into a Teflon lined autoclave and heated at 200 °C for 24 h and cooled naturally to obtain the black precipitate. Then, the precipitate was washed three times with deionized water and dried in vacuum at 80 °C overnight. The g-C_3N_4 loading percentages were 10, 20, and 30% and they denoted as CSC10, CSC20, and CSC30 nanocomposites, respectively. The pure $CuCo_2S_4$ was also prepared under same condition without the addition of g-C_3N_4.

2.3 Characterization

The phase structure and purity were analysed using X-ray diffraction (XRD). The XRD patterns were recorded using X-ray diffractometer (Rigaku) with Cu Kα radiation (λ = 1.5418 Å) at a scan rate of 2 °C/min. Morphology of the samples was observed with a field emission scanning electron microscopy, Zeiss EVO18 electron microscope and a transmission electron microscopy, JEOL JEM 2100 microscope. The chemical composition of the samples investigated by X-ray photoelectron spectroscopy (XPS) equipped with X-ray source with energy of 1489.7 eV, using Scienta omicron GMBH instrument. UV–vis diffuse reflectance spectra (UV–vis DRS) were analysed using Jasco V-750 diffuse reflectance spectrophotometer. The change in dye concentration during the degradation process was analysed by a Shimadzu UV-1700 spectrophotometer.

2.4 Photocatalytic Studies

The photocatalytic studies were carried out in a typical visible-light photo reactor under room temperature using 300 W halogen lamp. In a typical process, 50 mg of the photocatalyst was suspended in 100 mL of 10 mg L^{-1} of MB solution and dispersed by ultrasonication. After that, the solution was stirred under dark condition for 20 min to attain the adsorption–desorption equilibrium between the dye solution and the photocatalyst. Then the light source was turned on to study the photodegradation reaction. In different reaction courses, 2 mL of the suspension was withdrawn and the suspension was centrifuged at 5000 rpm to obtain the clear solution and the absorbances were analysed using the spectrophotometer.

3 Results and Discussion

The powder XRD patterns of $CuCo_2S_4$ and CSC nanocomposites are illustrated in Fig. 1a, b. The characteristic peak of pure g-C_3N_4 at 27.5° attributes to the (002) plane (Fig. 1a). For the $CuCo_2S_4$ powder, the diffraction peaks at 26.6°, 31.3°, 38.0°, 47.0°, 49.9°, and 54.8° are corresponding to the (022), (113), (004), (224), (115), and (044) planes of cubic $CuCo_2S_4$, respectively (JCPDS Card no. 42-1450) [21]. There is no other impurity peak corresponding to D-penicillamine, which ascertains the phase purity of the synthesized samples. Furthermore, the peaks of both g-C_3N_4 and $CuCo_2S_4$ co-existed in the CSC nanocomposites, which confirm that g-C_3N_4 was successfully incorporated into $CuCo_2S_4$ matrix (Fig. 1b).

The FT-IR spectra of g-C_3N_4, $CuCo_2S_4$, and CSC nanocomposites are illustrated in Fig. 2. The broad band around 3100–3300 cm^{-1} corresponds to the N–H stretching vibration. In addition, the peak at 812 cm^{-1} corresponds to the breathing mode of s-triazine, whereas the peaks in the region of 1240–1650 cm^{-1} are due to the stretching vibrations of aromatic C–N heterocycles (Fig. 2a) [22–25]. For the pure $CuCo_2S_4$, the peak at 623 cm^{-1} is ascribed to the vibration of Cu-S and the peak at 1243 cm^{-1} is related to the Co-S bond [26]. In Fig. 2c, all the characteristic peaks of g-C_3N_4 and $CuCo_2S_4$ are observed, which further confirms successful incorporation of g-C_3N_4 and $CuCo_2S_4$ counterparts.

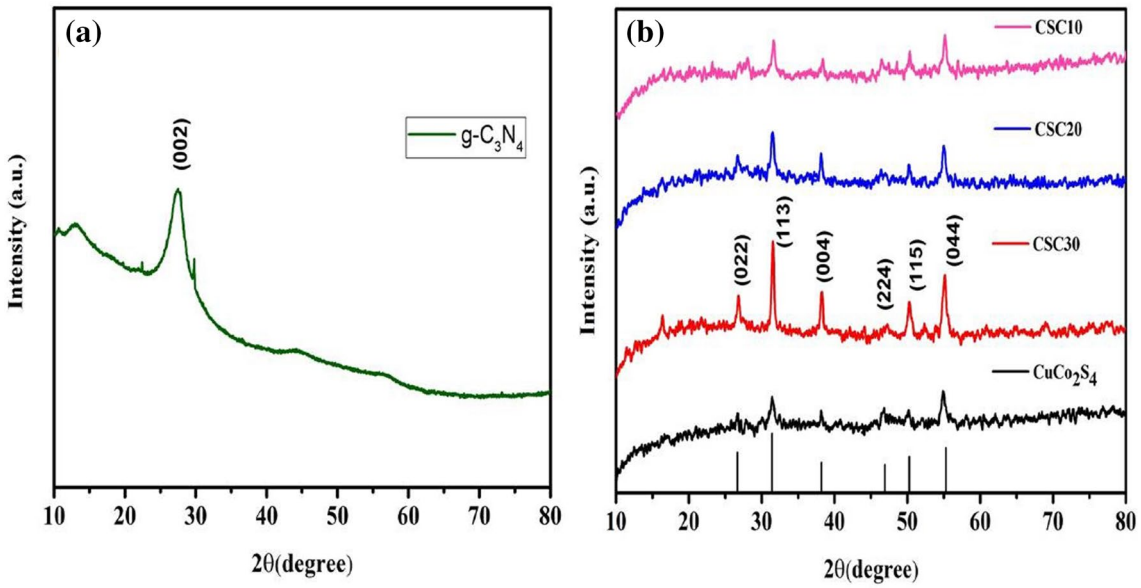

Fig. 1 XRD patterns of the **a** g-C_3N_4 and **b** $CuCo_2S_4$, CSC10, CSC20, and CSC30 nanocomposites

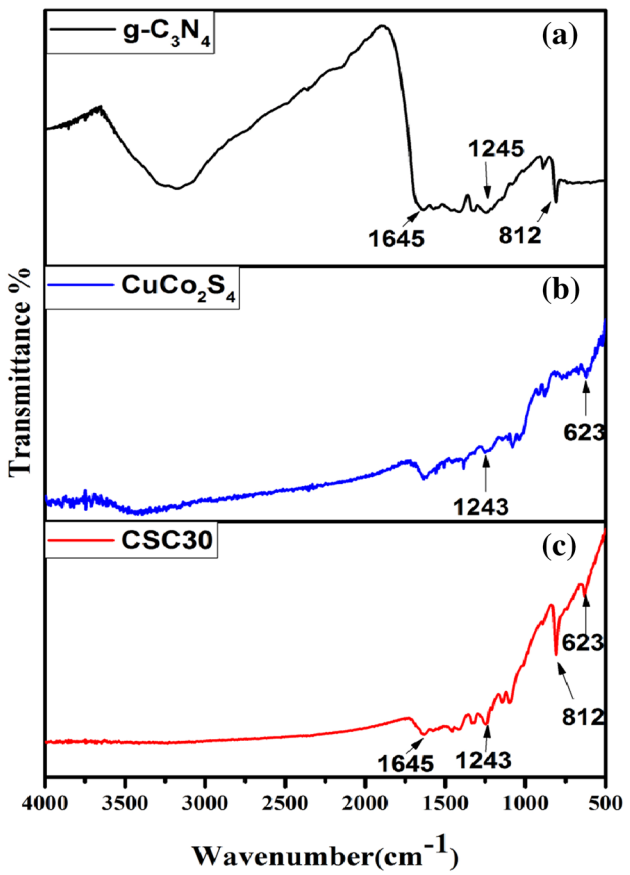

Fig. 2 FT-IR spectra of the **a** g-C_3N_4, **b** $CuCo_2S_4$, and **c** CSC30 nanocomposite

Morphology of the fabricated samples was investigated by FESEM analysis. Figure 3a, b shows the FESEM image of pure $CuCo_2S_4$, which confirms that the sample is composed of spongy sphere like morphology. Figure 3c shows that the bulk g-C_3N_4 has composed of unique sheet like morphology. Figure 3d displays anchoring of $CuCo_2S_4$ particles on the surface of g-C_3N_4 sheets, which prevents further agglomeration of $CuCo_2S_4$ particles. This is highly beneficial for the superior charge separation in the $CuCo_2S_4$ particles. Thus FESEM and HRTEM studies are in good agreement with XRD and FT-IR analysis. The SAED pattern of the CSC30 nanocomposite in Fig. 3f indicates the polycrystalline nature of $CuCo_2S_4$ with interplanar distance 0.279 nm, which perfectly matched with (004) diffraction patterns of $CuCo_2S_4$.

The composition of the prepared the CSC30 nanocomposite was analysed by the EDS elemental technique. Figure 4a–g clearly indicates the presence of only C, N, Cu, Co, and S elements. The signals for C and N elements originated from g-C_3N_4 and the peaks for Cu, Co, and S elements are from $CuCo_2S_4$ counterparts of the nanocomposite.

To further confirm the composition and chemical states of the CSC30 nanocomposite, XPS analysis was carried out.

The survey scan displays the presence of main elements including Cu, Co, S, C, and N, which further confirms the results of EDX analysis (Fig. 5a). The high resolution XPS spectrum of Cu 2p shows broad peaks at 932.7 and 952.7 eV correspond to Cu $p_{3/2}$ and Cu $2p_{1/2}$, which indicates the oxidation state of Cu is +2 (Fig. 5b). The spectrum of Co 2p (Fig. 5c) shows two peaks at 778 and 793.2 eV correspond to Co $2p_{3/2}$ and Co $2p_{1/2}$, which

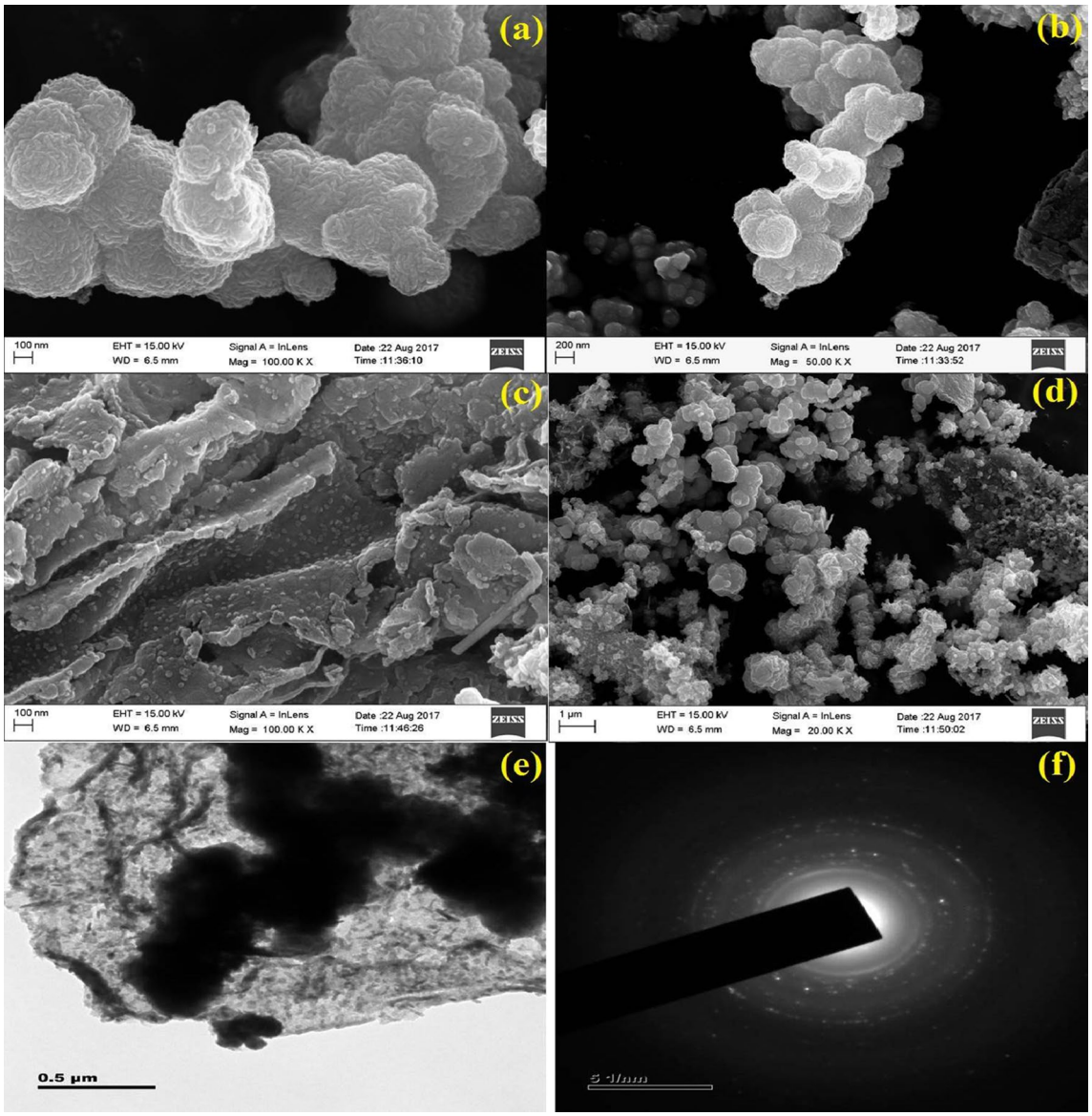

Fig. 3 FESEM images of the **a, b** pure $CuCo_2S_4$, **c** pure g-C_3N_4, and **d** CSC30 nanocomposite, **e** TEM image and **f** SAED pattern of the CSC30 nanocomposite

confirms the existence of both Co^{2+} and Co^{3+} oxidation states of Co. In the S 2p spectrum (Fig. 5d), the peak at 162 eV indicates the existence of sulphur in S^{2-} oxidation state [21]. In C 1 s spectrum (Fig. 5e), peak at 284.5 eV corresponds to C–C bond and the second peak at 287 eV belongs to sp^3 hybridised carbon in C–N group of g-C_3N_4. The N 1 s spectrum (Fig. 5f) is deconvoluted into three different peaks. The peak observed at 397.9 eV corresponds to the sp^2 hybridised aromatic N atom (C–N=C) and the peak at 399.7 eV belongs to the N atom that involved in the bridging of three carbon atom N–$(C)_3$. Finally the peak observed at 402.3 eV corresponds to the amino C–N–H group [27]. Thus, the elemental composition and chemical states in the CSC30 nanocomposite are confirmed by XPS analysis.

UV–vis DRS technique was used to analyse the optical properties of the prepared samples. The band gap energy of the prepared samples was evaluated using the following equation [28].

$$\alpha h\nu = \mathrm{B}\left(h\nu - E_g\right)^{n/2} \quad (1)$$

where, $h\nu$ is the photoenergy, α is absorption coefficient, B is proportionality constant, n is related to the transition type and ν is the light frequency. As observed in Fig. 6a, the g-C_3N_4 shows strong absorption with an absorption edge

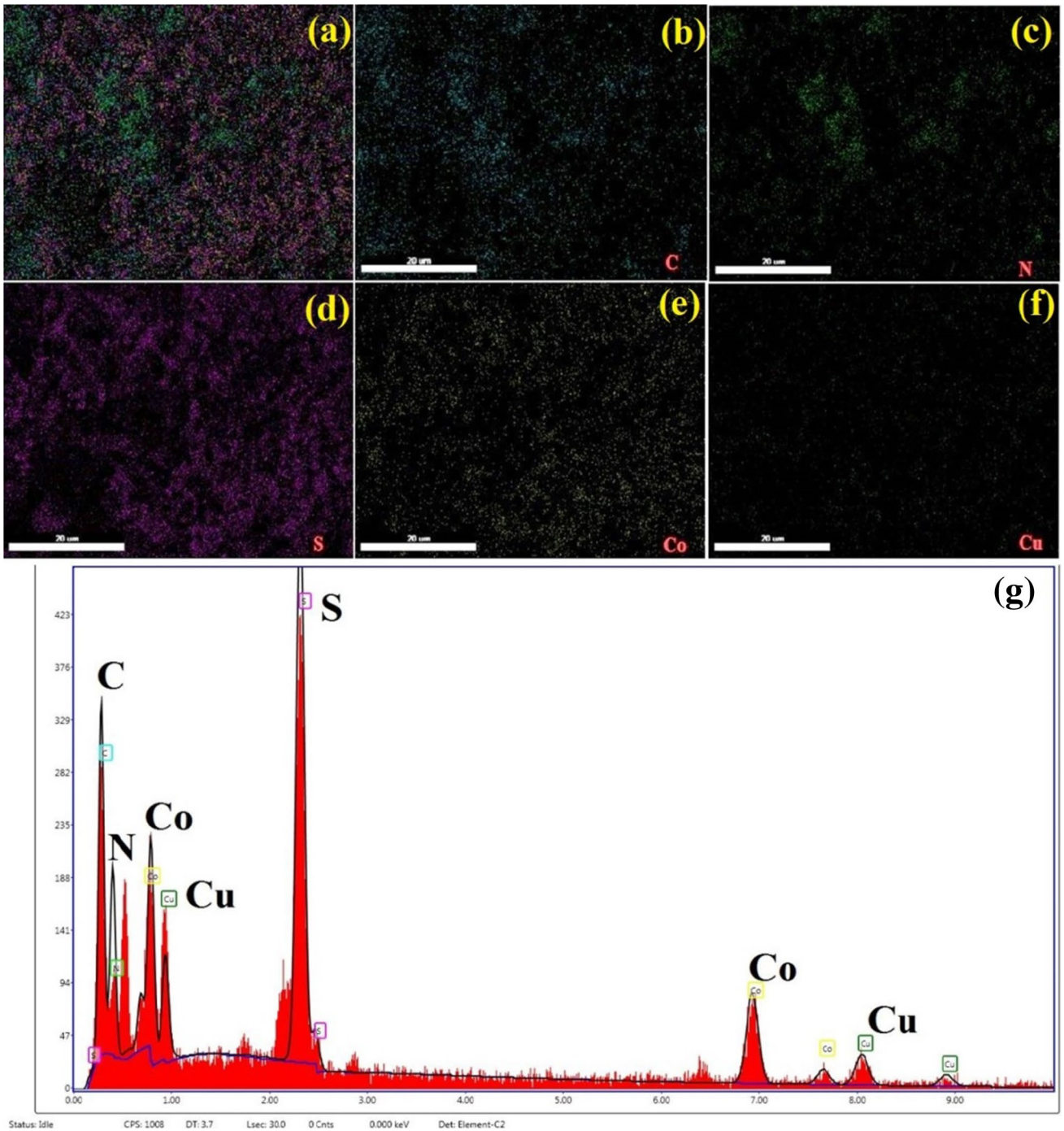

Fig. 4 **a–g** Elemental mapping images of different elements and EDX spectrum for the CSC30 nanocomposite

nearly at 460 nm and the $CuCo_2S_4$ powder shows substantial absorption in the whole range of visible light. Figure 6b illustrates band gap calculations for the fabricated samples. It is evident that band gaps of the $CuCo_2S_4$, g-C_3N_4, CSC10, CSC20, and CSC30 are 1.4, 2.74, 1.2, 1.06, and 1.01 eV, respectively. The low band gaps of the CSC nanocomposites indicates that these photocatalysts could have remarkable photocatalytic performance under visible light.

The transient photocurrent studies of the $CuCo_2S_4$ and CSC30 nanocomposite are shown in Fig. 7. Both of the $CuCo_2S_4$ and CSC30 nanocomposite show fast photochemical current responses under visible light.

The CSC30 nanocomposite exhibits the strongest photoelectrochemical activity, whose photocurrent density is higher than that of the pure $CuCo_2S_4$. This is mainly due to the proper loading of g-C_3N_4 on the surface of the $CuCo_2S_4$,

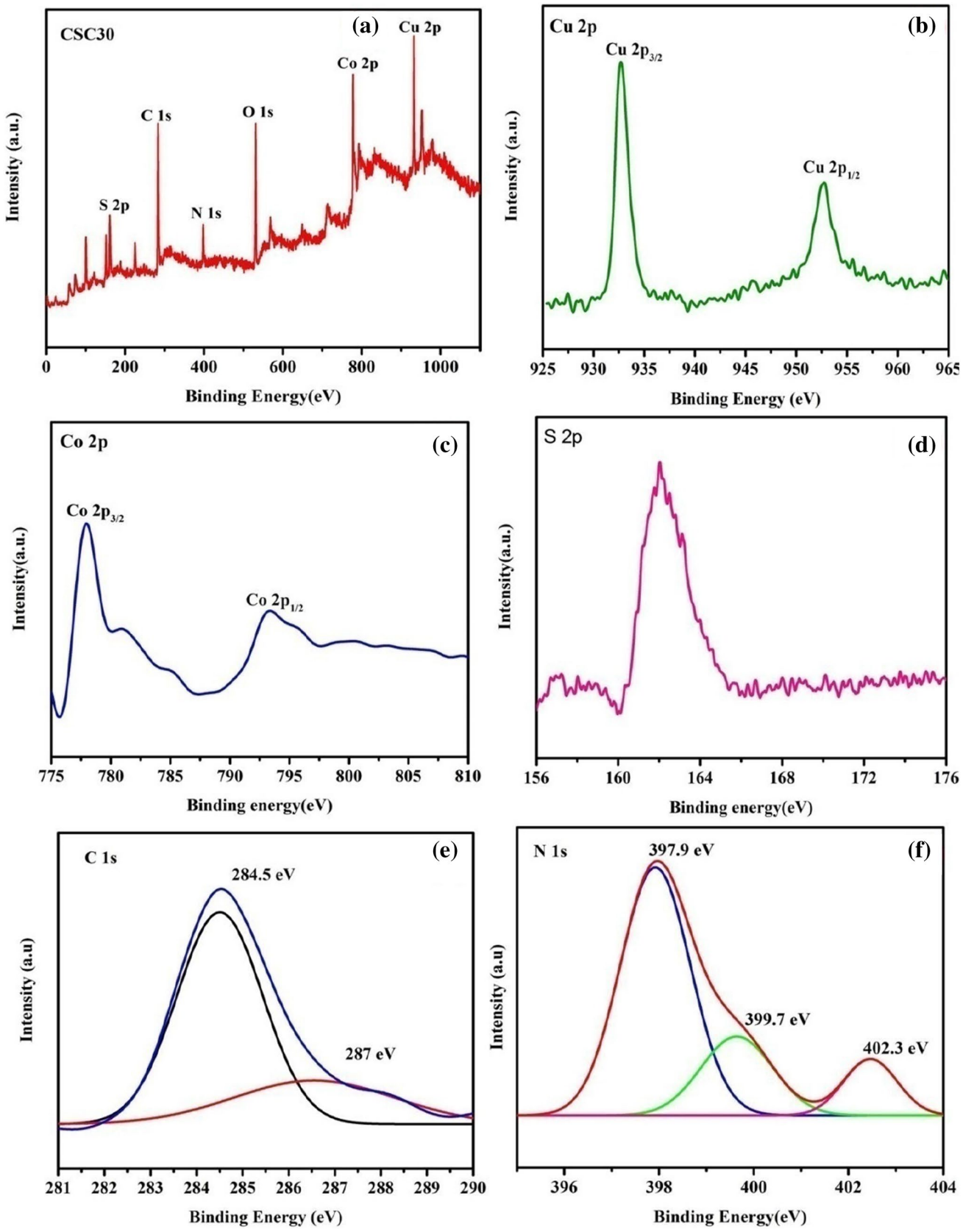

Fig. 5 XPS spectra of the CSC30 nanocomposite: **a** survey scan, **b** Cu2p, **c** Co 2p, **d** S2p, **e** C1s, and **f** N1s

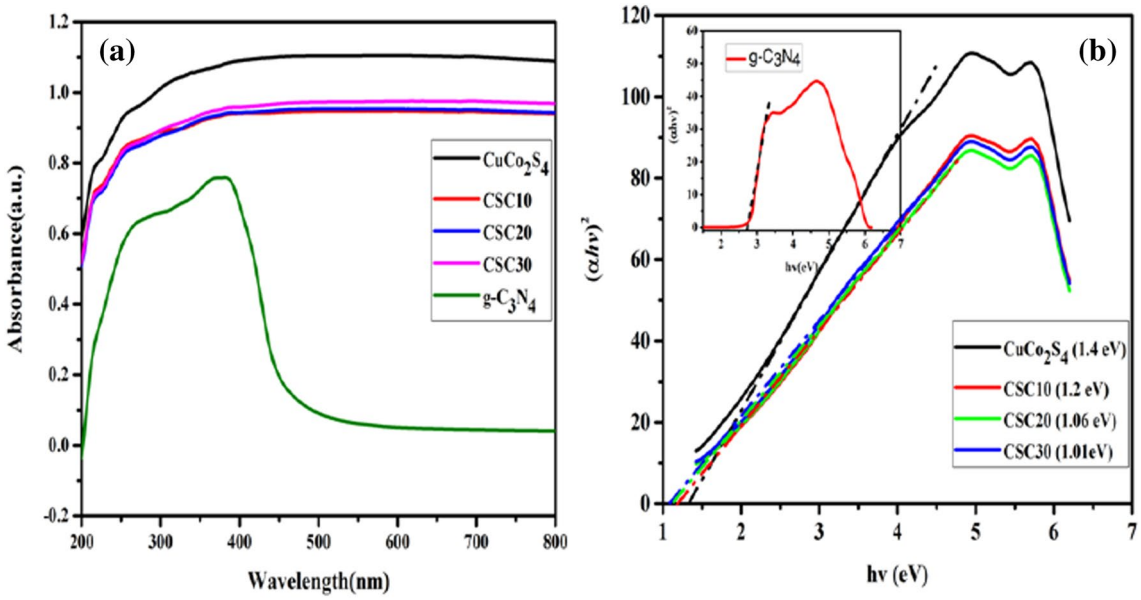

Fig. 6 UV–vis DRS spectra of the g-C_3N_4, $CuCo_2S_4$, CSC10, CSC20 and CSC30 nanocomposites

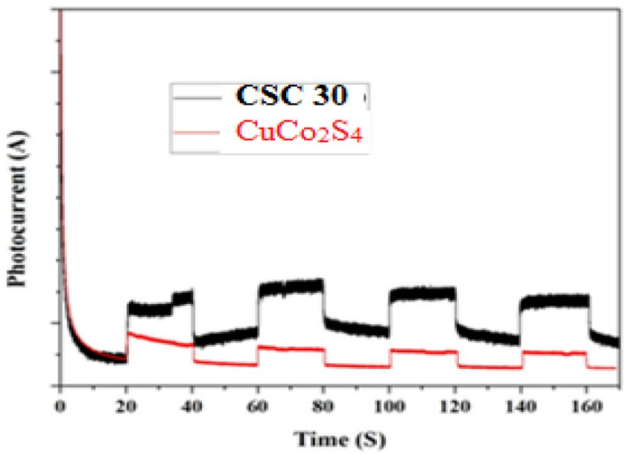

Fig. 7 Photocurrent responses for the $CuCo_2S_4$ and CSC30 nanocomposite

leading to an effective heterojunction structure which acts as good conducting pathway for electron transportation in the photocatalytic process.

3.1 Photocatalytic Activity

The photocatalytic degradation process was studied by examining the absorbance changes of MB under visible-light irradiation. Figure 8a illustrates temporal UV–vis spectra for MB during the degradation reaction over the CSC30 nanocomposite. As can be seen, the pollutant is nearly degraded after the light irradiation for 180 min. Figure 8b shows the C/C_0 of MB as a function of irradiation time over the $CuCo_2S_4$ and CSC nanocomposites where C is the concentration with respect to time (t) and C_0 is the initial concentration of MB. Figure 8b shows that in the absence of any photocatalyst, there is no degradation of MB dye. It is clear that photocatalytic activity of the nanocomposites are obviously higher than that of the pure $CuCo_2S_4$. The degradation efficiency was nearly 90, 88, 80, and 65% for the CSC30, CSC20, CSC10, and $CuCo_2S_4$, respectively. Figure 8c shows that the degradation efficiency increases with an increase g-C_3N_4 loading. This is due to easier transport of the charge carriers created by the effective incorporation of g-C_3N_4, as confirmed by transient photocurrent studies. The important factor that determines the commercialization of a photocatalyst is the stability and reusability. Hence, recycling experiments were carried out to check stability of the photocatalyst. Three cycles of degradation studies were carried out using over the CSC30 nanocomposite as photocatalyst under the same conditions. The photocatalytic degradation ability of the CSC30 nanocomposite was slightly decreased in the third degradation cycle and it retained nearly 83% of its activity as shown in the (Fig. 8d). Thus, the CSC30 nanocomposite shows good photocatalytic stability and reusability for the photocatalytic applications.

3.2 Photocatalytic Mechanism

In photocatalytic processes, photocatalytic performance is mainly dependent to the increase in production of electron–hole pairs and suppression of them from fast recombination. Using the relation proposed by Butler and Ginley [29, 30], the conduction band (CB) and valence band (VB)

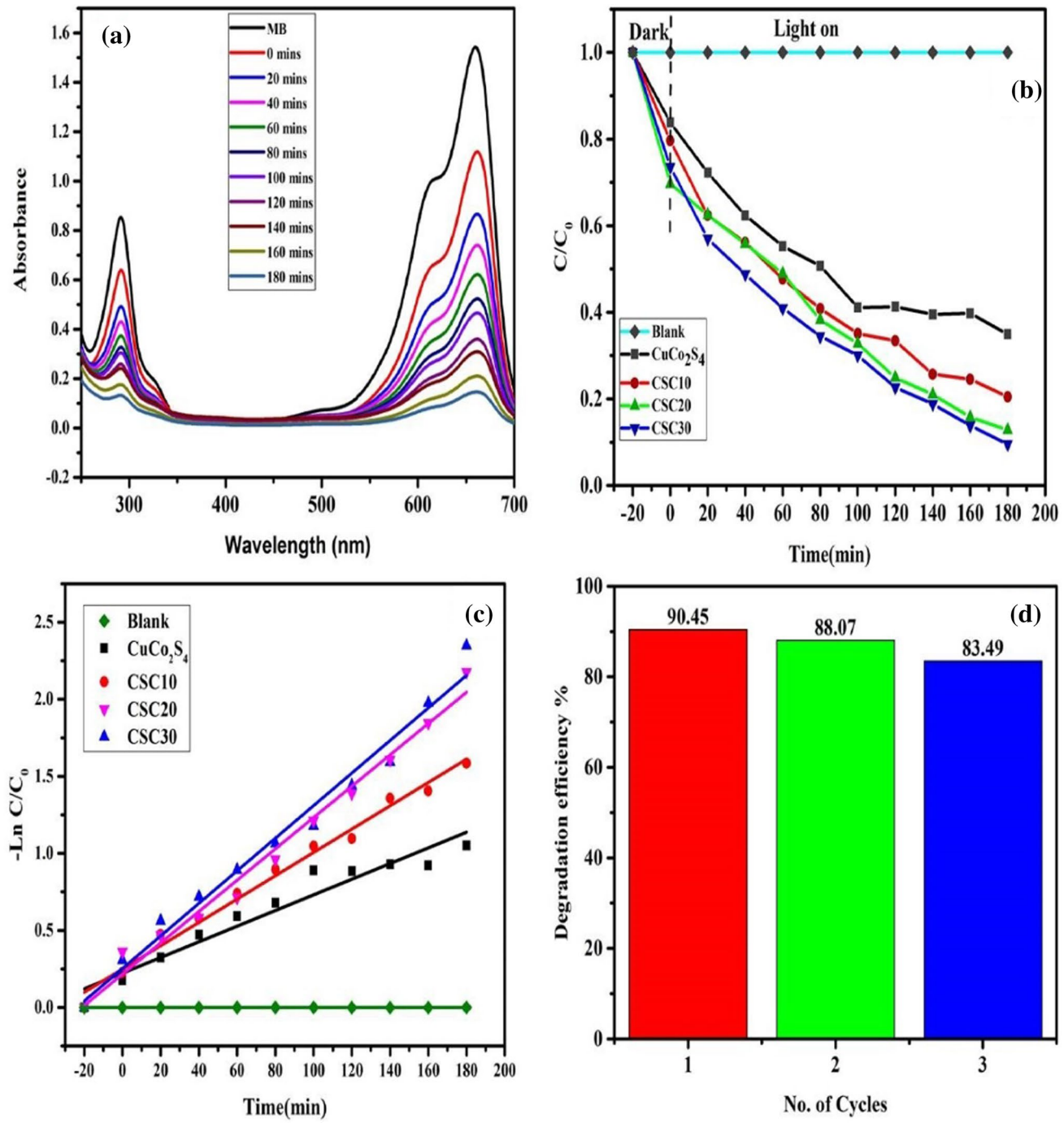

Fig. 8 **a** Temporal UV–vis spectra of MB during the degradation reaction over the CSC30 nanocomposite. **b** Photocatalytic degradation of MB over the $CuCo_2S_4$ and CSC nanocomposites. **c** Plots for LnC/C_0 versus irradiation time for different photocatalysts. **d** Stability test of the CSC30 nanocomposite towards MB degradation upon three cycles

potentials of the semiconductors presented in the CSC nanocomposites were calculated.

$$E_{CB} = \chi - E^e - 0.5E_g \quad (2)$$

$$E_{VB} = E_{CB} - E_g \quad (3)$$

where E_{VB} is the VB potential and E_{CB} is the CB potential, E^e is the energy of free electrons on the hydrogen scale, E_g is band gap of the semiconductor, and χ is the absolute electronegativity, which calculated by the following equation [31].

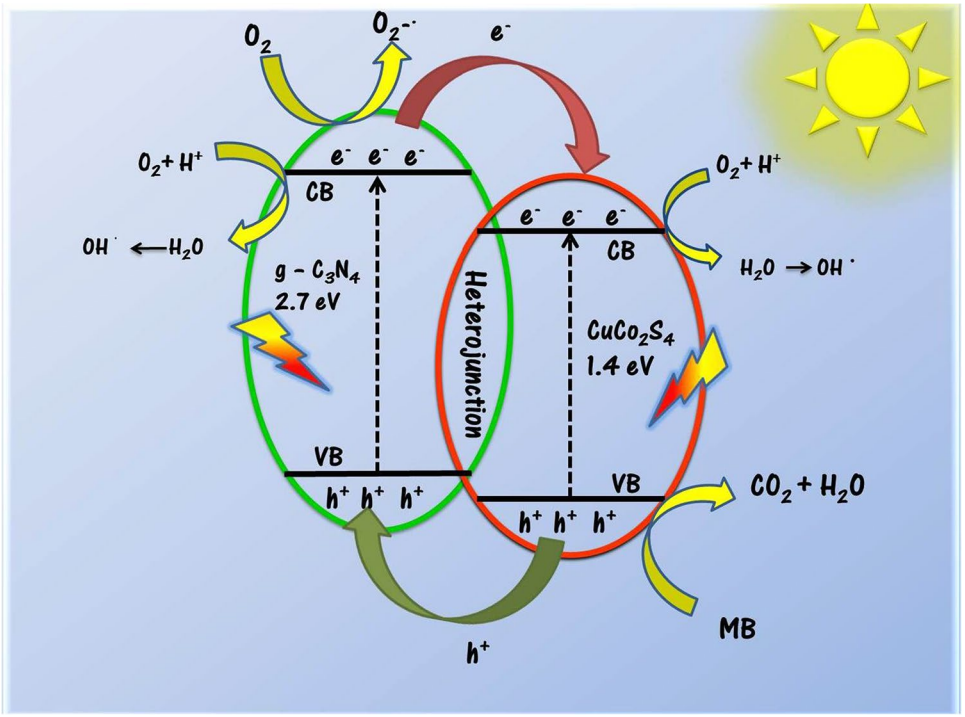

Fig. 9 The proposed photocatalytic mechanism for photodegradation of MB by the CSC30 nanocomposites

$$\chi = \left(x(A)^a x(B)^b x(C)^c\right)^{1/(a+b+c)} \quad (4)$$

where a, b, and c are the number of atoms in the semiconductor. For g-C_3N_4, E_g is 2.74 eV and χ is 4.67 eV. The calculated E_{CB} and E_{VB} are − 1.22 and 1.48 eV, respectively. For the $CuCo_2S_4$, E_g is 1.4 eV, χ is 5.32 eV, E_{CB} and E_{VB} were calculated to be 0.13 and 1.53 eV, respectively. Under visible-light irradiation, $CuCo_2S_4$ and g-C_3N_4 absorb visible light to produce the charge carriers. The CB edge potential of g-C_3N_4 is quite higher than that of $CuCo_2S_4$. As a consequence, the excited electrons transfer from the CB of g-C_3N_4 to that of $CuCo_2S_4$ and the holes generated in the VB of $CuCo_2S_4$ migrate to the VB of g-C_3N_4. The schematic diagram for the proposed mechanism is illustrated in Fig. 9. Based on this mechanism, electrons are successfully separated from the holes, which leads to the increased photocatalytic activity for the CSC nanocomposites [32, 33].

4 Conclusions

In this work, we synthesized novel biomolecule-assisted method for preparation of the CSC nanocomposites using D-penicillamine by simple solvothermal method and their photocatalytic activities were investigated towards MB degradation under visible light. Different characterization techniques confirmed formation of heterojunction between $CuCo_2S_4$ and g-C_3N_4, which was effective in separation of the photoinduced charge carriers. It was found that photocatalytic performance of the nanocomposites are higher than the pure $CuCo_2S_4$ powder. Finally, a realistic mechanism was proposed for the enhanced photocatalytic activity using potential edge energies of the semiconductors presented in the nanocomposite.

Acknowledgements This work was financially supported by DST- Science and Engineering Research Board (SERB) India, under "Early Career Research Award Scheme" (ECR/2016/001535/CS) to Dr. S. Vadivel.

References

1. X. Zhang, S. Li, S. Hu, J. Chen, W. Jiang, J. Zhang, L. Ji, ,L. Cai, Y. Wang, W. Song, J. Liu, Mater. Lett. **185**, 50 (2016)
2. Y. Zhang, G. Zhu, M. Hojamberdiev, J. Gao, J. Hao, J. Zhou, P. Liu, Appl. Surf. Sci. **371**, 231 (2016)
3. Q. Zhang, B. Xu, S. Yuan, M. Zhang, T. Ohno, Catal. Today **284**, 27 (2017)
4. J. Chen, W. Mei, Q. Huang, N. Chen, C. Lu, H. Zhu, J. Chen, W. Hou, J. Alloy. Compd. **688**, 225 (2016)
5. D. Maruthamani, D. Divakar, M. Kumaravel, J. Ind. Eng. Chem. **30**, 33 (2015)
6. A. Senthilraja, B. Subash, B. Krishnakumar, D. Rajamanickam, M. Swaminathan, M. Shanthi, Mat. Sci. Semicon. Proc. **22**, 83 (2014)
7. T. Li, X. Hu, C. Liu, C. Tang, X. Wang, S. Luo, J. Mol. Catal. A-Chem. **425**, 124 (2016)
8. S. Yang, C. Chen, L. Liu, L. Zhu, X. Xu, Mater. Res. Bull. **92**, 29 (2017)
9. C. Yu, K. Wang, P. Yang, S. Yang, C. Lu, Y. Song, S. Dong, J. Sun, J. Sun, Appl. Surf. Sci. **420**, 233 (2017)

10. H. Fakhri, A.R. Mahjoub, A.H. Cheshme Khavar, Appl. Surf. Sci. **318**, 65 (2014)
11. T.Y. Ho, L.Y. Chen, Energy Procedia **61**, 2050 (2014)
12. J. Ye, T. Chen, Q. Chen, W. Chen, Z. Yu, S. Xu, J. Mater. Chem. A **4**, 13194 (2016)
13. S. Vadivel, D. Maruthamani, B. Paul, S.S. Dhar, A. Habibi-Yangjeh, S. Balachandran, B. Saravanakumar, A. Selvakumar, K. Selvam, RSC Adv. **6**, 74177 (2016)
14. R.H. Fath, S.J. Hoseini, New J. Chem. **41**, 3392 (2017)
15. M. Mousavi, A. Habibi-Yangjeh, S.R. Pouran, J. Mater. Sci.: Mater. Electron. (2017). doi.https://doi.org/10.1007/s10854-017-8166-x
16. Q. Liu, Y. Guo, Z. Chen, Z. Zhang, X. Fang, Appl. Catal. B-Environ. **183**, 231 (2016)
17. S. Vadivel, D. Maruthamani, A. Habibi-Yangjeh, B. Paul, S.S. Dhar, K. Selvam, J. Colloid Interf. Sci. **480**, 126 (2016)
18. X. Fang, J. Song, H. Shi, S. Kang, Y. Li, G. Sun, L. Cui, Int. J. Hydrogen Energ. **42**, 5741 (2017)
19. A. Akhundi, A. Habibi-Yangjeh, J. Colloid Interf. Sci. **504**, 697 (2017)
20. K. Vignesh, M. Kang, Mater. Sci. Eng. B- Adv. **199**, 30 (2015)
21. J. Tang, Y. Ge, J.F. Shen, M. Ye, Chem. Commun. **52**, 1509 (2016)
22. G. Zhang, J. Zhang, M. Zhang, X. Wang, J. Mater. Chem. **22**, 8083 (2012)
23. J. Sun, Y. Yuan, L. Qiu, X. Jiang, A. Xie, Y. Shen, J. Zhu, Dalton Trans. **41**, 6756 (2012)
24. G. Liao, S. Chen, X. Quan, H. Yu, H. Zhao, J. Mater. Chem. **22**, 2721 (2012)
25. M. Lu, Z. Pei, S. Weng, W. Feng, Z. Fang, Z. Zheng, M. Huang, P. Liu, Phys. Chem. Chem. Phys. **16**, 21280 (2014)
26. J. Shen, J. Tang, P. Dong, Z. Zhang, J. Ji, R. Baines, M. Ye, RSC Adv. **6**, 13456 (2016)
27. S. Tonda, S. Kumar, Y. Gawli, M. Bhardwaj, S. Ogale, Int. J. Hydrogen Energ. **42**, 5971 (2017)
28. M. Mousavi, A. Habibi-Yangjeh, M. Abitorabi, J. Colloid Interf. Sci. **480**, 218 (2016)
29. M.A. Butler, D.S. Ginley, J. Electrochem. Soc. **125**, 228 (1978)
30. A. Habibi-Yangjeh, M. Shekofteh-Gohari, Sep. Purif. Technol. **184**, 334 (2017)
31. W. Zhang, X. Xiao, L. Zheng, C. Wan, Appl. Surf. Sci. **358**, 468 (2015)
32. J. Fu, Y. Tian, B. Chang, F. Xi, X. Dong, J. Mater. Chem. **22**, 21159 (2012)
33. T. Xian, H. Yang, L.J. Di, J.F. Dai, J. Alloy. Compd. **622**, 1098 (2015)